JACS
JOURNAL OF THE AMERICAN CHEMICAL SOCIETY
Article
pubs.acs.org/JACS

Structural Transitions from Triangular to Square Molecular Arrangements in the Quasi-One-Dimensional Molecular Conductors $(DMEDO\text{-}TTF)_2XF_6$ (X = P, As, and Sb)

Takashi Shirahata,*[†,‡] Keita Shiratori,[‡] Shouhei Kumeta,[§] Tadashi Kawamoto,[§] Tadahiko Ishikawa,[‡] Shin-ya Koshihara,[‡] Yoshiaki Nakano,[¶] Hideki Yamochi,[¶] Yohji Misaki,[†] and Takehiko Mori[‡,§]

[†]Department of Applied Chemistry, Graduate School of Science and Engineering, Ehime University, 3 Bunkyo-cho, Matsuyama, Ehime 790-8577, Japan

[‡]Department of Chemistry and Materials Science, Graduate School of Science and Engineering, Tokyo Institute of Technology, O-okayama 2-12-1, Meguro-ku, Tokyo 152-8552, Japan

[§]Department of Organic and Polymeric Materials, Graduate School of Science and Engineering, Tokyo Institute of Technology, O-okayama 2-12-1, Meguro-ku, Tokyo 152-8552, Japan

[¶]Research Center for Low Temperature and Materials Sciences, Kyoto University, Sakyo-ku, Kyoto, 606-8501, Japan

S *Supporting Information*

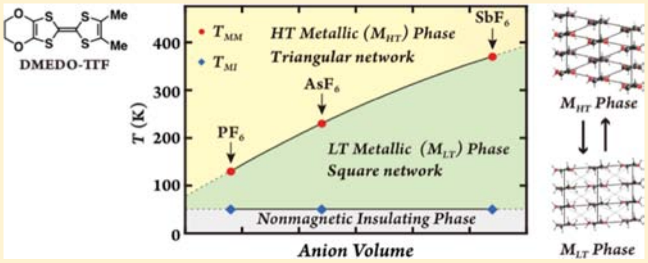

ABSTRACT: A series of quasi-one-dimensional molecular conductors $(DMEDO\text{-}TTF)_2XF_6$ (X = P, As, and Sb), where DMEDO-TTF is dimethyl(ethylenedioxy)tetrathiafulvalene, undergo characteristic structural transitions in the range of 130−195 K for the PF_6 salt and 222−242 K for the AsF_6 salt. The dramatic structural transition is induced by the order of the ethylenedioxy moiety, and the resulting anion rotation leads to the reconstruction of the H···F interaction between the methyl groups and the anions. The unique hydrogen bonds play a crucial role in the transition. As a result, the molecular packing is rearranged entirely; the high-temperature molecular stacks with an ordinary quasi-triangular molecular network transforms to a quasi-square-like network, which has never been observed among organic conductors. Nonetheless, the low-temperature phase exhibits a good metallic conductivity as well, so the transition is a metal−metal (MM) transition. The resistivity measured along the perpendicular direction to the conducting *ac*-plane ($\rho_\perp$) and the calculation of the Fermi surface demonstrate that the high-temperature metal phase is a one-dimensional metal, whereas the low-temperature metal phase has considerable interchain interaction. In the SbF_6 salt, a similar structural transition takes place around 370 K, so that the quasi-square-like lattice is realized even at room temperature. Despite the largely different MM transition temperatures, all these salts undergo metal−insulator (MI) transitions approximately at the same temperature of 50 K. The low-temperature insulator phase is nonmagnetic, and the reflectance spectra suggest the presence of charge disproportionation with small charge difference (0.14).

1. INTRODUCTION

Among the quasi-one-dimensional (Q1D) molecular conductors based on the tetrathiafulvalene (TTF) derivatives,[1−4] TMTTF and TMTSF-based organic conductors (TMTTF = tetramethyltetrathiafulvalene and TMTSF = tetramethyltetraselenafulvalene) are one of the most extensively studied compounds, because a large variety of electronic states including charge order (CO), spin-Peierls, antiferromagnetic, spin-density-wave, and superconducting states have been realized, and the universal phase diagram correlating these electronic states to the external pressure and the counteranions has been investigated.[5] Another Q1D conductor, $(EDO\text{-}TTF)_2PF_6$ (EDO-TTF = ethylenedioxy-TTF), reveals a different aspect owing to the characteristic cooperative metal−insulator (MI) transition at 279 K, to which the Peierls, CO, and anion ordering instabilities are related at the same time.[6,7] The structural change occurs from an almost uniform molecular stack in the high-temperature phase to a tetramerized stack with [BFFB] periodicity in the low-temperature phase, where B and F represent the bent and flat molecules and their charges are almost 0 and +1, respectively. Despite the quarter-filled one-dimensional electronic nature, this transition results in formation of a [0, +1, +1, 0] type CO pattern and the strongest transfer integral exists between two adjacent monovalent molecules, which is unusual in molecular conductors.[7,8] On account of the cooperative nature of the MI transition, this compound exhibits a spectacular ultra-fast photo-induced phase transition (PIPT), where the insulating state transforms to a metal-like state upon laser irradiation.[9] At

Received: April 10, 2012
Published: July 20, 2012

the early stage of the PIPT, the [0, +1, +1, 0] type CO pattern changes to a nonequilibrium [+1, 0, +1, 0] type CO state.[10]

These studies indicate that most of the Q1D molecular conductors show an inherent multistability, the stable states included in which exhibit the differences in multiple physical properties. The sensitivity to the external stimuli such as magnetic fields,[1] physical and chemical pressure,[5] and laser light[9] is also a characteristic feature of materials in this category. These materials can be applied to organic electronic devices and study of these materials contributes to enabling improvements to be made to the performance of such devices. To achieve the functionalities based on the multistable nature, it is essential to tune the balance of the Coulomb interaction and transfer integrals by using chemical modifications of the donor molecules and the counteranions.[11] As an analogue of (EDO-TTF)$_2$PF$_6$, (MeEDO-TTF)$_2$PF$_6$ (MeEDO-TTF = monomethyl-EDO-TTF, Chart 1) shows a molecular packing motif different from (EDO-TTF)$_2$PF$_6$ with a two-dimensional electronic structure.[12−15] This system shows a first-order semiconductor−semiconductor transition associated with charge disproportionation.[13] Fabre and co-workers have reported synthesis and properties of dimethyl-EDO-TTF (DMEDO-TTF) as well as the preparation of its cation radical salts.[16,17] (DMEDO-TTF)$_2$PF$_6$ exhibits a first-order structural phase transition at 130 K, but neither the detail of the transport properties, crystal structures at high- and low-temperature phases, nor the mechanism of the phase transition has been investigated probably due to the destructive structural transition. The investigation of the mechanism of the first-order structural phase transition could offer a new insight into the nature of peculiar structural transitions, which have been observed in molecular conductors based on the EDO-containing donors, including BO-based organic superconductors (BO = bis(ethylenedioxy)-TTF).[18]

Chart 1

X = S: TMTTF
X = Se: TMTSF

R^1 = R^2 = H: EDO-TTF
R^1 = H, R^2 = Me: MeEDO-TTF
R^1 = R^2 = Me: DMEDO-TTF

As a candidate of multistable electronic system, we have prepared (DMEDO-TTF)$_2$XF$_6$ (X = P, As, and Sb) by electrocrystallization, and their transport, magnetic, and structural properties are investigated as well as the optical property of (DMEDO-TTF)$_2$PF$_6$. It is revealed that the structural phase transition is accompanied by a huge rearrangement of the donor packing pattern. Although there are very few examples of molecular conductors in which a dramatic change of molecular arrangement is fully identified both above and below the structural transition, it has been reported in (BEDT-TTF)$_2$Br$_{1.3}$I$_{1.1}$Cl$_{0.6}$ (BEDT-TTF = bis(ethylenedithio)-tetrathiafulvalene) that the high-temperature β''-phase transforms to the low-temperature α-like phases.[19] The present system is furthermore notable because both phases are metallic conductors, and hence, the structural transition is a metal−metal (MM) transition. Here, we present the change of various physical properties across the MM transition as well as the low-temperature ground state below the additional MI transition at 50 K.

2. EXPERIMENTAL SECTION

2.1. Sample Preparation. DMEDO-TTF was synthesized according to the literature method.[16] The X-ray diffraction experiment of DMEDO-TTF was carried out on a Rigaku VarimaxSutarn CCD system at the Integrated Center for Science, Ehime University. Crystal structure analysis of DMEDO-TTF was summarized in Table S1 and Figure S1 (Supporting Information). Single crystals of (DMEDO-TTF)$_2$PF$_6$ (typical size: 0.80 × 0.16 × 0.05 mm^3) were prepared by electrochemical oxidation of a chlorobenzene solution containing DMEDO-TTF (5−7 mg) and tetra-*n*-butylammonium hexafluorophosphate as a supporting electrolyte (50−65 mg). Electrocrystallizations of the new salts (DMEDO-TTF)$_2$XF$_6$ (X = As and Sb; typical size: 2.00 × 0.12 × 0.02 mm^3) were carried out in ethanol solutions of DMEDO-TTF (7 mg) and the corresponding tetra-*n*-butylammonium salts (18−21 mg). Platinum electrodes (1.0 mm ϕ wire) and standard H-shaped cells were employed, and a constant current of 0.1 μA was applied at 20 °C for 2−3 weeks.

2.2. Transport Property. Electrical resistivities were measured by the conventional four-probe method using low-frequency AC current. Gold wires (10 μm ϕ diameter) were attached to a single crystal using carbon paste, and silver paste was used to connect the gold wires to the measurement substrate. For the PF$_6$ and AsF$_6$ salts, measurements were carried out parallel and perpendicular to the conducting *ac*-plane, and the resistivity of the SbF$_6$ salt was measured parallel to the conducting *ac*-plane. Parallel resistivities ($\rho_{//}$) were measured along the crystal long axis, which corresponds to molecular stacking axis (crystallographic *c* axis) and perpendicular resistivities ($\rho_{\perp}$) were measured along the thickness of the plate-like crystals (crystallographic *b* axis).

2.3. Magnetic Property. Static magnetic susceptibilities (χ_{p}) were measured on a Quantum Design SQUID magnetometer (MPMS-5) by applying a DC magnetic field of 10 kOe. The correction of the core diamagnetism was evaluated with Pascal's table. ESR measurements were carried out for single crystals using an X-band spectrometer (JEOL JES-TE100). The scan width of the magnetic field and the *g*-values were calibrated by the spectra of Mn^{2+}/MgO with a hyperfine structure constant of 86.77 Oe and g_0 of 2.00094. The ESR spectra of (DMEDO-TTF)$_2$PF$_6$ at room temperature were summarized in Figures S2 and S3 (Supporting Information). The ESR line shape was a symmetric Lorentzian. The line width (ΔH_{pp}) of (DMEDO-TTF)$_2$PF$_6$ at room temperature varies from 4.5 to 5.0 Oe and the maximum of ΔH_{pp} was observed by applying the magnetic field parallel to the *a** axis. Therefore, the ESR measurements at various temperatures were performed with the magnetic field parallel to the *a** axis.

2.4. Optical Property. Temperature dependence of the optical reflectivity spectra in the mid-IR range (0.08−1.0 eV) was measured by using Fourier type infrared spectrometer (ThermoFisher Nicolet 840). The light was linearly polarized parallel and perpendicular to the molecular stacking axis on the *ac* plane using the wire-grid type polarizer. Gold mirror was used as a reference mirror. The sample was in the conduction type cryostat (Oxford, Microstat).

2.5. X-ray Crystal Structure Analysis. The diffraction data of the XF$_6$ (X = P, As, and Sb) salts at room temperature, the AsF$_6$ salt at 100 K, and the SbF$_6$ salt at 373 K were collected on a Rigaku AFC7R diffractometer with graphite monochromated Mo Kα radiation (0.71069 Å) and a rotating anode generator. Empirical psi-scan absorption corrections[20] were applied for the PF_6 and SbF_6 salts, and no absorption correction was applied for the AsF_6 salt. The diffraction data of the PF_6 salt at 100 K were collected on a Bruker AXS APEX-II CCD system with graphite monochromatized Mo Kα radiation (0.71073 Å). Since the crystal of the PF_6 salt usually broke, we used a crystal coated with Apiezon N grease and Araldite epoxy resin. Raw frame data were integrated using SAINT[21] and empirical absorption correction using SADABS[22] was applied. The crystal structures were solved by the direct method (SIR2008[23]) and refined by full-matrix least-squares on F^2 (SHELXL-97[24]). The hydrogen atoms of the ethylenedioxy groups were introduced in the calculated positions (HFIX 23, riding model), while the positions of the hydrogen atoms of the methyl groups were calculated using the HFIX 137 instruction.

2.6. Band Calculation. From the results of the X-ray crystal structure analyses, intermolecular overlap integrals were calculated using highest occupied molecular orbitals (HOMOs) of DMEDO-TTF obtained by the extended Hückel MO calculations using semiempirical parameters for Slater-type atomic orbitals listed in Table S2 (Supporting Information). It has been assumed that the transfer integral (t) is proportional to the overlap integral (S), $t = ES$ ($E = -10$ eV). The electronic band dispersions and Fermi surfaces were calculated using the intermolecular transfer integrals under the tight-binding approximation.[25]

3. RESULTS AND DISCUSSION

3.1. Transport Properties. Fabre and co-workers have reported a first-order structural transition of $(DMEDO\text{-}TTF)_2PF_6$ at around 130 K, but the details of the low-temperature transport properties have not been investigated due to the crystal's fragility at the phase transition.[17] We also have found serious difficulty in measuring the low-temperature transport properties because the crystal usually breaks when cooled across the transition. By covering the crystal with Apiezon N grease and/or using very slow cooling (ca. -0.1 K min^{-1}), we have finally succeeded in measuring the transport properties.

Figure 1 shows temperature dependence of the parallel resistivity ($\rho_{//}$) of $(DMEDO\text{-}TTF)_2XF_6$ (X = P, As, and Sb) measured by the four-probe method. The current is applied along the crystal long axis, which corresponds to the molecular stacking axis ($//c$). The PF_6 and AsF_6 salts exhibit a metallic resistivity around room temperature, and the room-temperature conductivities are 120 S cm^{-1} for the PF_6 salt and 420 S cm^{-1} for the AsF_6 salt. These salts undergo a MM transition at 130 K for the PF_6 salt and 230 K for the AsF_6 salt with a discontinuous jump of the resistivity. At the MM transition, the crystals of the PF_6 salt usually break (see video in Supporting Information), while the AsF_6 salt crystals bend. Although a dramatic structural change occurs in these salts, the change seems less destructive in the AsF_6 salt. The resistivity usually jumps downward in the PF_6 salt and upward in the AsF_6 salt, but the magnitude is somewhat dependent on the samples.

The resistivity of the SbF_6 salt is nearly constant around room temperature, but increases gradually from room temperature to 250 K. The resistivity becomes more flat but slowly increases from 250 to 50 K, in contrast to the decreasing resistivity in the low-temperature metal region of the other salts. This salt is, however, considered to be essentially metallic down to 50 K in view of the magnetic properties (vide infra). When heated above room temperature, the SbF_6 salt shows a structural transition at around 370 K, but the shape of the crystal does not change at this temperature. Around this temperature, the resistivity is not measured with sufficient reproducibility owing to the damage to the contacts.

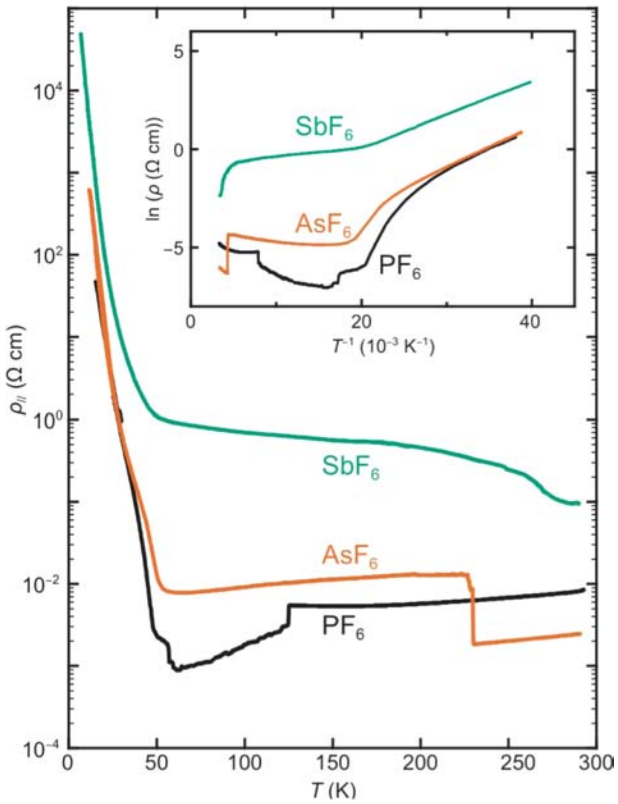

Figure 1. Temperature dependence of the parallel resistivity ($\rho_{//}$) of the PF_6 (black line), AsF_6 (orange line), and SbF_6 (green line) salts measured along the stacking axis ($//c$). The inset shows the Arrhenius plots.

The PF_6, AsF_6, and SbF_6 salts show sharp MI transitions at 50 K. The activation energies (E_a) of the PF_6, AsF_6, and SbF_6 salts are estimated to be 240, 210, and 170 K, respectively, from the Arrhenius plots (inset of Figure 1) in the temperature region between 25 and 40 K. It is remarkable that the low-temperature MI transition temperatures (T_{MI}) are almost the same for all salts, and the E_a values below T_{MI} are close to each other. An analogous anion size effect on the MM and MI phase transitions has been reported in $(DMEDO\text{-}TSeF)_2XF_6$ (DMEDO-TSeF = dimethyl(ethylenedioxy)-tetraselenafulvalene, X = P, As, and Sb).[26] In this case, the MM transition is observed only for X = P and the insulator states are observed for X = As and Sb. The difference of the anion size effect between DMEDO-TTF and DMEDO-TSeF is derived from the selenium substitution in the central tetrachalcogenofulvalene moiety. The small sulfur atoms reduce the intermolecular interaction, and therefore, the metallic phase becomes relatively unstable in the DMEDO-TTF system. In $(DMEDO\text{-}TSeF)_2PF_6$, the structure of the low-temperature phase has not been known, but the lattice constants show a dramatic change at the MM transition, so it is expected that the low-temperature phase has an entirely rearranged molecular network similarly to the present compounds.

The resistivities measured along the perpendicular direction to the conducting ac-plane ($\rho_\perp$) of $(DMEDO\text{-}TTF)_2XF_6$ (X = P, As, and Sb) (~10^{-2} S cm^{-1}) are by 4 orders of magnitude smaller than the parallel conductivities. The anisotropic properties of the PF_6 and AsF_6 salts indicate the low-dimensional electronic nature. The perpendicular resistivities ($\rho_\perp$) exhibit different behavior from the $\rho_{//}$. As shown in Figure 2, semiconducting behavior is observed above the MM transition temperature (T_{MM}) in the PF_6 salt, but the AsF_6 salt exhibits temperature independent $\rho_\perp$. A similar behavior has been observed in the Q1D molecular conductor $(TMTSF)_2PF_6$,[27] and this has been considered to be an evidence of the one-dimensional metallic nature at around room temperature. Below T_{MM}, $\rho_\perp$ shows metallic behavior similar to $\rho_{//}$, indicating higher dimensionality in the low-temperature metallic (M_{LT}) phase. The increase in dimensionality of the M_{LT} phase is associated with the structural transition from the one-dimensional high-temperature metallic (M_{HT}) phase to quasi-one-dimensional M_{LT} phase with enhanced interchain interaction.

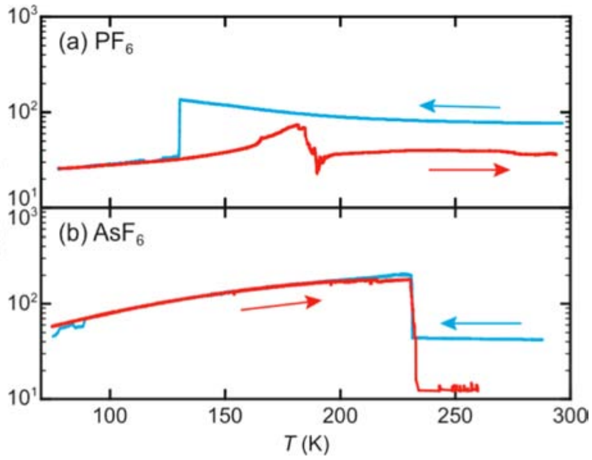

Figure 2. Temperature dependence of the perpendicular resistivity ($\rho_\perp$) of (a) the PF_6 and (b) AsF_6 salts measured perpendicular to the conducting *ac*-plane. Blue and red lines represent cooling and heating runs, respectively.

For the PF_6 salt, enormous resistivity hysteresis is observed in the range of 130−195 K, indicating that the MM transition is a first-order transition. On the other hand, the resistivity anomaly of the AsF_6 salt appears at around 230 K for both cooling and heating runs, though differential scanning calorimetry (DSC) measurement reveals that the phase transition of the AsF_6 salt involves a latent heat and a hysteretic nature in the range of 222−242 K (Figure S4 in Supporting Information). The structural transition enthalpies of cooling and heating runs are −6.0 and 6.8 kJ mol^{-1} at the DSC peak temperatures of 227 and 235 K, respectively. Therefore, the MM transition of the AsF_6 salt is also a first-order transition.

3.2. Magnetic Properties. To clarify the origin of the MM and MI phase transitions, ESR and SQUID measurements have been performed. Figure 3 shows temperature dependence of the integrated ESR intensity, which corresponds to relative spin susceptibility (χ_{spin}), and line width (ΔH_{pp}) for the PF_6, AsF_6, and SbF_6 salts when the magnetic field is applied parallel to the a^* axis for the PF_6 and AsF_6 salts and the b^* axis for the SbF_6 salt. Although ΔH_{pp} tends to decrease with decreasing the temperature, it shows an abrupt upward jump at the MM transition. At T_{MM}, the χ_{spin}'s of the PF_6 and AsF_6 salts show anomalies, but the *g*-values do not show any obvious change.

The static magnetic susceptibility (χ_p) is measured by the SQUID technique for the three salts. The room temperature χ_p values of the PF_6 and AsF_6 salts are 3.6×10^{-4} and 3.0×10^{-4} emu mol^{-1}, respectively, which are reasonable as the Pauli paramagnetism in a TTF-based molecular metal. Although small anomaly is observed, χ_p shows basically temperature-independent behavior down to 50 K in accordance with the metallic conducting behavior in the same temperature range. The χ_p of the PF_6 salt shows an upturn at 140 K, and the maximum susceptibility is observed at 130 K. The temperature of maximum susceptibility is in good agreement with T_{MM} observed in the resistivity measurement. The hysteresis is observed in the range of 130−195 K in the same way as the resistivity measurement. The anomaly indicates the difference of the electronic states between the M_{HT} and M_{LT} phases, where the magnitude of the Pauli paramagnetism is in

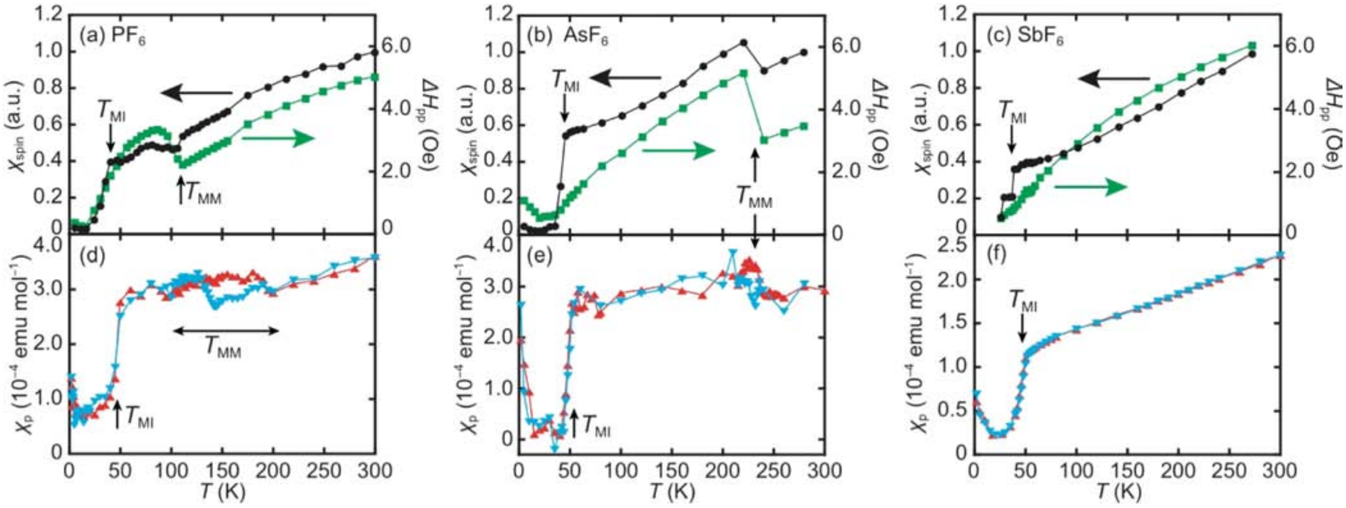

Figure 3. Temperature dependence of ESR integrated intensity (relative spin susceptibility, χ_{spin}, black circle) and line width (ΔH_{pp}, green square) for (a) the PF_6 (H // a^*), (b) AsF_6 (H // a^*), and (c) SbF_6 salts (H // b^*), as well as the static magnetic susceptibility (χ_p, blue inverted triangle and red triangle) measured by the SQUID technique for (d) the PF_6, (e) AsF_6, and (f) SbF_6 salts. Blue inverted triangles and red triangles represent cooling and heating runs, respectively.

proportion to the density of states (DOS) at around the Fermi level. The χ_{spin} of the PF_6 salt shows a small drop at T_{MM} differently from χ_{p}. In the AsF_6 salt, the static susceptibility exhibits a similar anomaly, but the magnitude of the Pauli paramagnetism is essentially the same both above and below the MM transition. The small change suggests the small difference of the DOS at around the Fermi level between the M_{HT} and M_{LT} phases.

For the SbF_6 salt, the static magnetic susceptibility is 2.3×10^{-4} emu mol^{-1} at room temperature, which is smaller than the corresponding values of the PF_6 and AsF_6 salts, and χ_{p} and χ_{spin} decrease gradually with decreasing temperature. The magnetic property of the SbF_6 salt above 50 K also does not conflict with the Pauli-like paramagnetic behavior in correspondence with the temperature-independent resistivity. At 50 K, the spin and the static susceptibilities of all salts drop sharply, leading to a nonmagnetic state. The charge-density-wave (CDW) formation is suggested as the origin of the MI transition. The rapid increase of χ_{p} below ~10 K is due to the contribution of the impurity spins.

3.3. Optical Property. Figure 4 shows reflectivity spectra of a $(\mathrm{DMEDO\text{-}TTF})_2PF_6$ single crystal in the M_{LT} and insulating phases. Electric field polarized perpendicular to the molecular stacking axis is used in order to observe intramolecular vibrational modes. In the M_{LT} phase at 80 K, a single peak is observed. This peak is assigned to the C=C stretching mode of 4,5-ethlylenedioxy-1,3-dithiole ring, since the normal mode calculation using the Gaussian03 (B3LYP/6-31G(d,p))[28] indicates a C=C stretching mode with strong transition dipole moment in this frequency range. The frequency of the C=C stretching mode in the DMEDO-TTF molecule is sensitive to the molecular charge and shifts to lower wavenumber in the oxidized states, since HOMO has bonding character at the C=C double bond according to the quantum chemical calculation (Figure 5). We can estimate the molecular charge of the DMEDO-TTF molecule judging from the frequency of these modes. Considering the metallic nature of this phase at 80 K, the molecular charge of the DMEDO-TTF molecule should be +0.5, then this single peak can be assigned to the C=C stretching mode of DMEDO-TTF$^{0.5+}$. At 20 K, two peaks are observed clearly. This peak splitting must be induced by the MI transition at 50 K. Then, two kinds of DMEDO-TTF molecules with different charges exist in the insulating phase. When there is perfect charge disproportionation as 2DMEDO-TTF$^{0.5+}$ → DMEDO-TTF^{0} + DMEDO-TTF^{+}, the expected splitting is 120 cm^{-1} from the quantum chemical calculation. The observed splitting is about 17 cm^{-1}, which is much smaller than the value of the entire charge disproportionation. The estimated charge difference is as small as 0.14 by assuming the linear relation between the charge and the frequency. Optical reflectivity with the linear polarized light $E \parallel$ stack showed a Drude-like reflectivity edge at around 1.0 eV above T_{MI} and the optical conductivity spectra deduced from the reflectivity spectra using Kramers−Kronig transformation demonstrate the absence of an energy gap in the M_{HT} and M_{LT} phases (Figure S5). This is probably further evidence for the metallic nature both above and below the structural transition. The optical and magnetic properties reveal that the MI transition in $(\mathrm{DMEDO\text{-}TTF})_2PF_6$ is ascribed to CDW formation accompanied by the singlet formation with small unequivalence of charges on respective molecules.

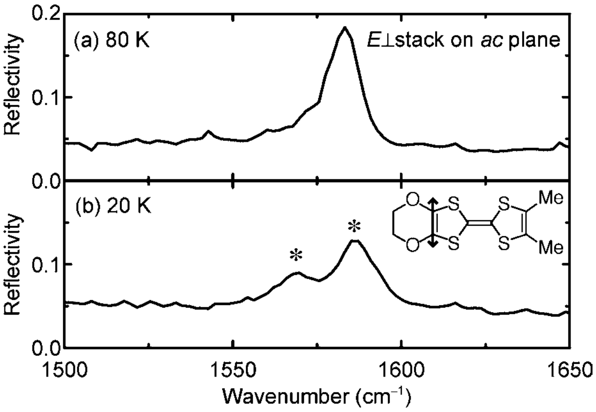

Figure 4. Reflectivity spectra of $(\mathrm{DMEDO\text{-}TTF})_2PF_6$ in (a) the low-temperature metallic (M_{LT}, 80 K) and (b) insulating (20 K) phases. The electric field was polarized perpendicular to the molecular stacking axis on the conducting *ac* plane.

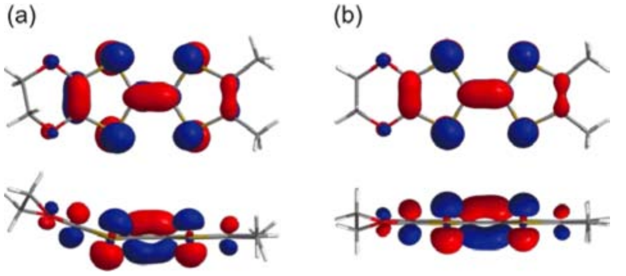

Figure 5. HOMO of DMEDO-TTF molecule calculated by the density functional theory (DFT) (B3LYP/6-31G(d,p)) based on the molecular structures determined by crystal structure analysis of (a) DMEDO-TTF at 100 K and (b) $(\mathrm{DMEDO\text{-}TTF})_2PF_6$ at 297 K.

3.4. Crystal Structure. X-ray crystal structure analyses were performed for the M_{HT} and M_{LT} phases of $(\mathrm{DMEDO\text{-}TTF})_2XF_6$ (X = P, As, and Sb). Table 1 lists the crystallographic data. Since the MM transitions of the PF_6 and AsF_6 salts take place at 130 and 230 K, the structure analyses of these salts are performed at 293 and 100 K for the M_{HT} and M_{LT} phases, respectively. While no unambiguous phase transition was observed by the resistivity measurement for the SbF_6 salt, the examination of temperature dependence of the lattice constants proved the discontinuous change around 370 K indicating a structural transition (Figure 6). Accordingly, the crystal structures are analyzed at 373 and 293 K, which correspond to the M_{HT} and M_{LT} phases, respectively.

All phases belong to triclinic space group $P\bar{1}$. Lattice parameters of the corresponding phases of the PF_6 and AsF_6 salts resemble each other. It is noteworthy that the lattice angles α and β are different by more than 10° between the M_{HT} and M_{LT} phases (Table 1); consequently, these phases are regarded as entirely different structures. At the transition from the M_{HT} phase to the M_{LT} phase, the *a* axes shrink, but the *b* axes expand. The anomalous change of the *b* axes, that is opposite to the thermal expansion, is ascribed to the rearrangement of mutual positions of the conducting layers. The lattice parameters of the SbF_6 salt at 293 K are similar to those of the M_{LT} phases of the PF_6 and AsF_6 salts, indicating that the phase of the SbF_6 salt at 293 K corresponds to the *low-temperature* metal (M_{LT}) phase of the other salts. The M_{HT} phases of the PF_6 and AsF_6 salts are isostructural to each other, but the M_{HT} phase of the SbF_6 salt is not strictly the same as

Table 1. Crystallographic Data of $(DMEDO\text{-}TTF)_2XF_6$ (X = P, As, and Sb)

	$(DMEDO\text{-}TTF)_2PF_6$		$(DMEDO\text{-}TTF)_2AsF_6$		$(DMEDO\text{-}TTF)_2SbF_6$	
formula	$C_{20}H_{20}O_4S_8PF_6$		$C_{20}H_{20}O_4S_8AsF_6$		$C_{20}H_{20}O_4S_8SbF_6$	
phase	M_{HT}	M_{LT}	M_{HT}	M_{LT}	M_{HT}	M_{LT}
T (K)	293	100	293	100	373	293
crystal system	Triclinic	Triclinic	Triclinic	Triclinic	Triclinic	Triclinic
space group	$P\bar{1}$	$P\bar{1}$	$P\bar{1}$	$P\bar{1}$	$P\bar{1}$	$P\bar{1}$
a (Å)	7.657(2)	7.536(5)	7.657(2)	7.573(9)	7.488(2)	7.886(3)
b (Å)	13.517(3)	13.99(1)	13.669(3)	14.17(2)	14.543(3)	14.398(3)
c (Å)	7.117(1)	6.899(5)	7.135(3)	6.910(5)	7.182(5)	7.076(3)
α (deg)	99.45(2)	89.05(1)	99.32(3)	88.68(7)	94.22(3)	90.58(2)
β (deg)	102.23(2)	114.137(9)	103.38(3)	114.23(6)	110.72(3)	117.22(2)
γ (deg)	74.82(2)	81.358(8)	74.64(2)	81.31(9)	78.96(2)	80.58(2)
V (Å^3)	690.1(3)	653.8(8)	696.5(4)	665.3(12)	718.0(5)	702.8(4)
Z	1	1	1	1	1	1
D_{calc} (g cm^{-3})	1.746	1.843	1.835	1.921	1.889	1.929
independent reflections	4002	2813	4062	3747	4195	4083
observed reflections [$I > 2\sigma(I)$]	2132	1707	2103	2944	2511	3187
$R1$; $wR2$ [$I > 2\sigma(I)$]	0.0570; 0.1532	0.0700; 0.1796	0.0525; 0.1227	0.1314; 0.3233	0.1164; 0.2924	0.0648; 0.1885
GOF	1.003	1.013	0.985	1.077	1.278	1.061

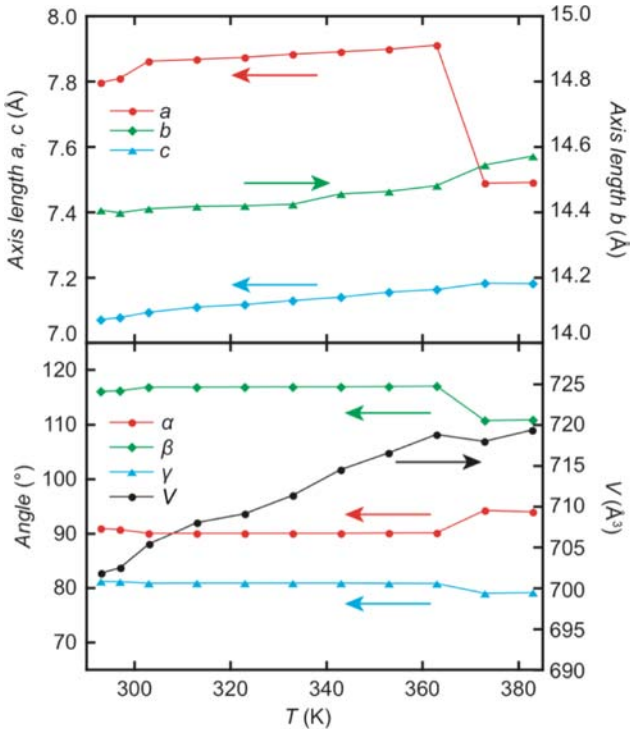

Figure 6. Temperature dependence of the lattice parameters for $(DMEDO\text{-}TTF)_2SbF_6$.

these phases; particularly, the lattice angles α, β, and γ of the SbF_6 salt are considerably different from those of the PF_6 and AsF_6 salts. Namely, the lattice angle α of the SbF_6 salt is smaller by 5° than those of the PF_6 and AsF_6 salts, whereas β and γ of the SbF_6 salt are larger by 4° and 10° than those of the PF_6 and AsF_6 salts. In general, the structural change at the transition is large in the PF_6 and AsF_6 salts in comparison with the SbF_6 salt, because the structural transition of the SbF_6 salt occurs at higher temperature. For example, α changes by ca. 10° in the PF_6 and AsF_6 salts, but by 4° in the SbF_6 salt. This is consistent with the tendency that the structural phase transitions are less dramatic in this order, and the crystals of the PF_6 and AsF_6 salts are likely to break at the transition.

The molecular packing motif of the M_{HT} phase of the PF_6 salt is shown in Figure 7 as a representative of the isostructural M_{HT} phases. To discuss small differences of the molecular packing, Table 2 lists geometrical parameters representing intermolecular interactions, together with transfer integrals calculated by molecular orbital calculation, where ϕ is an angle of the intermolecular vector from the molecular plane, x is the slip distance along the molecular long axis, and z is the interplanar distance between the molecular planes (Figure S7 in Supporting Information).[29] The DMEDO-TTF molecule, in which the terminal ethylene bridge shows disorder due to the flipping, is located on a general position, and a PF_6 anion is located at a center of inversion. A unit cell contains two donor molecules and one PF_6 anion, affording the donor to anion ratio of 2:1. The donor molecules in the M_{HT} phase at room temperature stack along the c axis in a head-to-tail manner with the interplanar distances z = 3.51 and 3.60 Å for the intermolecular interactions $c1$ and $c2$ of the PF_6 salt, and z = 3.50 and 3.62 Å for $c1$ and $c2$ of the AsF_6 salt. The slip distances x of $c1$ and $c2$ are 1.16 and 0.82 Å for the PF_6 salt and 1.20 and 0.74 Å for the AsF_6 salt, respectively (Table 2). The transfer integrals of $c1$ and $c2$ are almost comparable with each other, although x of $c2$ is smaller than that of $c1$. The small difference in the transfer integrals of $c1$ and $c2$ indicates very weak dimerization. The interaction a corresponds to translation along the crystal a axis, and their geometric parameters ϕ of the PF_6 and AsF_6 salts are around 12°. The relationship between the overlap integral (S) and the molecular geometry (ϕ) have been calculated, and zero crossing points of S are generated near ϕ = 12, 45, and 70°.[29] In consequence, the transfer integral a is very small. The crystal packing geometry is essentially equivalent to $(TMTSF)_2XF_6$[5,30] and $(EDO\text{-}TTF)_2PF_6$,[6] and the molecular arrangement is regarded as a quasi-triangular network similarly to other organic conductors.

The molecular arrangement of the M_{LT} phase of the PF_6 salt is depicted in Figure 8. The geometrical parameters and the transfer integrals of the AsF_6 salt are almost the same as those of the PF_6 salt (Table 2). For this reason, we discuss the PF_6 salt as a representative of the isostructural M_{LT} phases. The interplanar distances z are 3.43 Å for $c1$ and 3.46 Å for $c2$ and the dimerization is also very small in the M_{LT} phase. Although

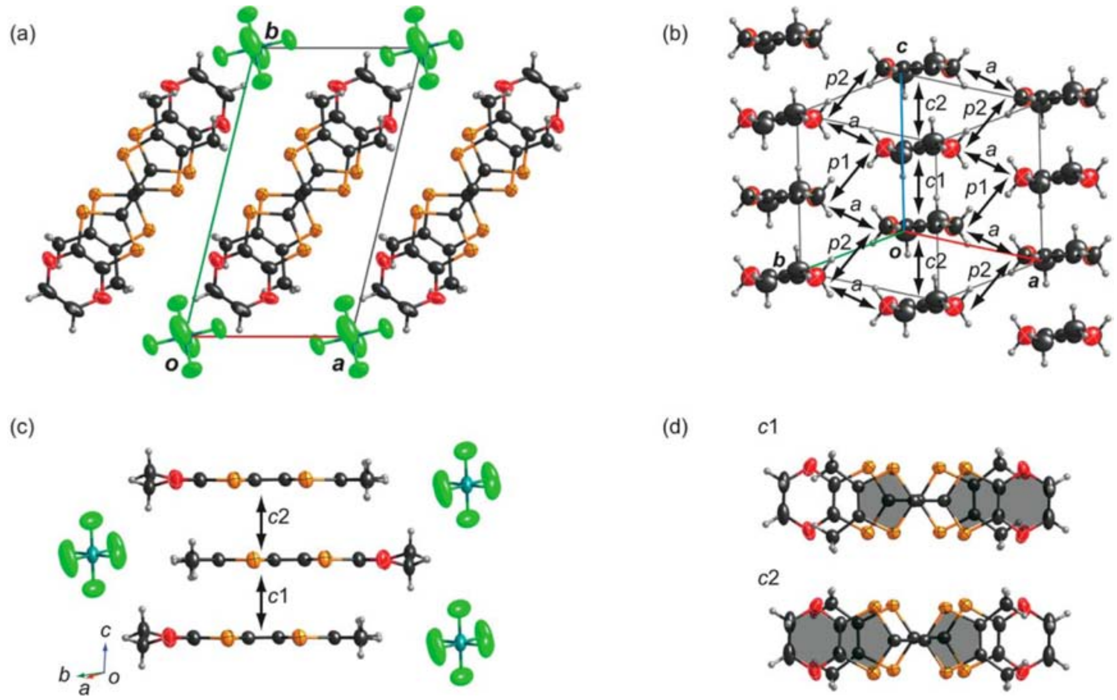

Figure 7. Molecular packing of the M_{HT} phase of the PF_6 salt viewed (a) along the *c* axis, (b) along the molecular long axis, (c) along the molecular short axis. (d) Molecular overlap modes for *c*1 and *c*2. The five- and six-membered rings of the top molecules are shaded. The minor orientations of the disordered ethylene bridge of the donor molecule are omitted for clarity.

Table 2. Transfer Integrals and Geometrical Parameters in $(DMEDO\text{-}TTF)_2XF_6$ (X = P, As, and Sb)[a]

	PF_6 M_{HT}				AsF_6 M_{HT}				SbF_6 M_{HT}			
	t (meV)	ϕ (deg)	*x* (Å)	*z* (Å)	*t* (meV)	ϕ (deg)	*x* (Å)	*z* (Å)	*t* (meV)	ϕ (deg)	*x* (Å)	*z* (Å)
*c*1	−265	89.1	1.16	3.51	−262	89.1	1.20	3.50	−233	88.3	1.27	3.56
*c*2	−269	88.7	0.82	3.60	−273	88.3	0.74	3.62	−234	88.4	1.26	3.62
a	−0.6	11.8	4.28	1.30	3.2	12.3	4.24	1.36	33	22.2	3.19	2.56
*p*1	−41	19.7	3.13	2.21	−41	19.1	3.04	2.14	29	9.2	1.92	1.00
*p*2	−21	20.6	5.11	2.30	−22	20.2	4.98	2.25	13	9.5	4.25	1.06
	PF_6 M_{LT}				AsF_6 M_{LT}				SbF_6 M_{LT}			
	t (meV)	ϕ (deg)	*x* (Å)	*z* (Å)	*t* (meV)	ϕ (deg)	*x* (Å)	*z* (Å)	*t* (meV)	ϕ (deg)	*x* (Å)	*z* (Å)
*c*1	−285	87.8	1.25	3.43	−283	88.0	1.22	3.44	−285	87.9	1.17	3.54
*c*2	−294	87.9	1.12	3.46	−286	87.7	1.14	3.47	−294	87.8	1.19	3.54
a	26	26.0	3.03	3.02	23	26.4	2.99	3.09	2.6	29.8	3.00	362
*p*1	104	3.9	1.78	0.41	101	3.3	1.78	0.35	104	0.8	1.84	0.09
*p*2	55	4.0	4.15	0.44	51	3.4	4.13	0.37	19	0.8	4.19	0.09
*p*3	10	32.0	2.90	3.87	10	31.4	2.91	3.82	4.7	28.6	3.03	3.45

[a] Definition of intermolecular interactions are depicted in Figure 7b and 8b, and definition of geometrical parameters are depicted in Figure S7.

the *x* value for *c*2 changes from 0.82 to 1.12 Å, the geometrical parameters for *c*1 and *c*2 are essentially the same for the M_{HT} and M_{LT} phases, so the structure of a single column is basically unchanged at the transition. By contrast, the molecules of the adjacent columns are aligned on the same level, as represented by the very small $\phi \sim 4°$ and $z \sim 0.4$ Å for *p*1 and *p*2. Accordingly, at the transition each column is regarded to move parallel to the stacking direction, corresponding to the considerable shift of the lattice constant β between the M_{HT} and M_{LT} phases. As shown in Figure 9 schematically, the M_{HT} phase has six neighboring molecules, and is regarded as a quasi-triangular molecular arrangement, whereas the M_{LT} phase constructs a quasi-square lattice, because there are eight neighboring molecules. Triangular molecular arrangement is universally observed in organic molecular crystals, because the well-known herringbone structure, the stacking structure, and the so-called κ-, β-, and β''-structures are all included in this category.[29,31] Therefore, the emergence of the square-like molecular arrangement is surprising. At the transition, each donor column also slips by 0.9−1.3 Å along the molecular long axis, as the *x* values of the interchain interactions *a*, *p*1, and *p*2 diminish from the M_{HT} phase values. Accordingly, it looks that the molecules rotate around each column (Figure 9b). The overall molecular rearrangements lead to the expansion of the lattice parameter *b* in the M_{LT} phase. The large molecular rearrangements are the reason that the crystals sometimes break or bend at the structural transition.

Together with the rearrangement of the donor packing pattern, the orientation of anion is also modulated at the MM transition. As shown in Figure 10, F1−P−F1* axis in the M_{HT}

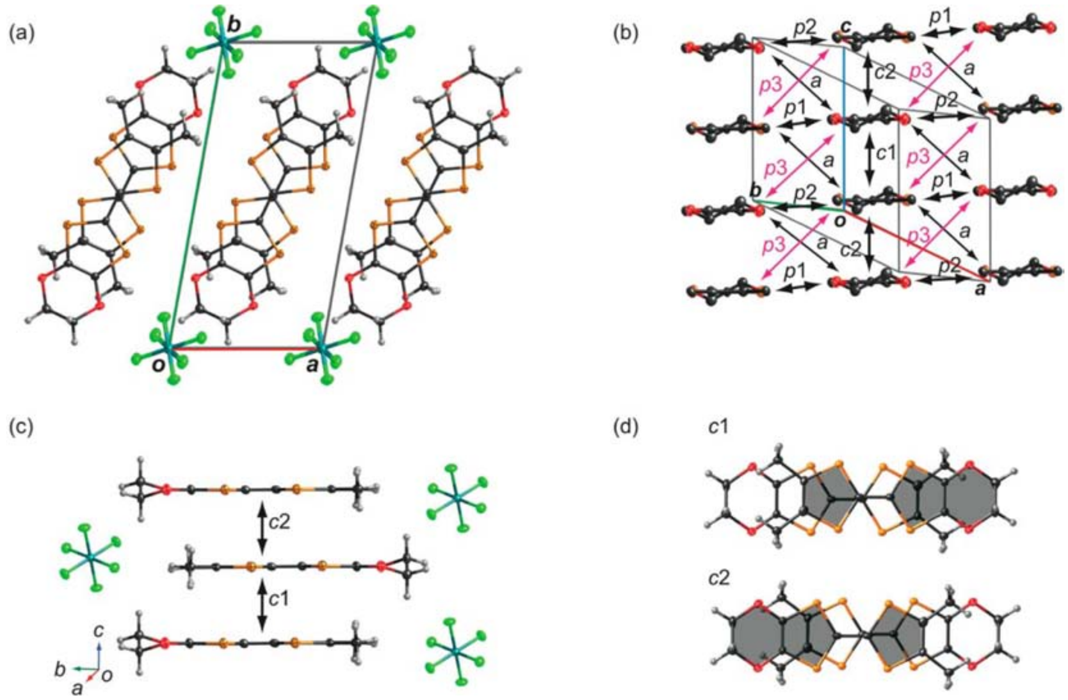

Figure 8. Molecular packing of the M_{LT} phase of the PF_6 salt viewed (a) along the *c* axis, (b) along the molecular long axis, (c) along the molecular short axis. (d) Molecular overlap modes for *c*1 and *c*2. The five- and six-membered rings of the top molecules are shaded. The hydrogen atoms in (b) are omitted for clarity.

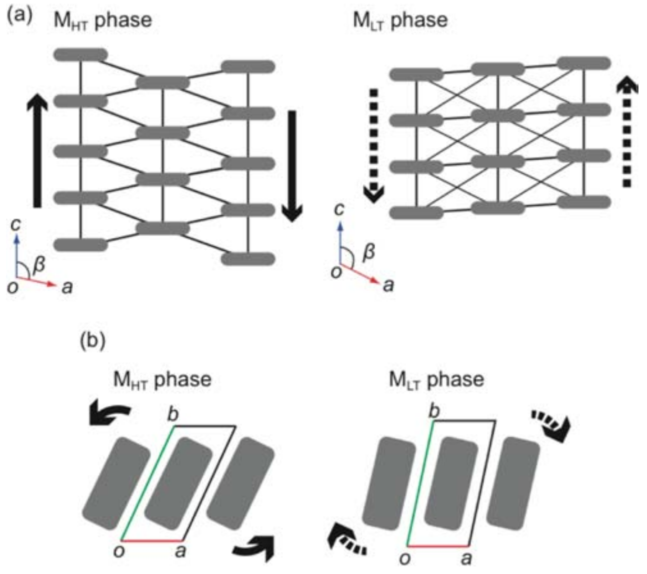

Figure 9. Schematic drawings of the structural transformation between the triangular arrangement with six neighboring molecules of the M_{HT} phase and the square arrangement with eight neighboring molecules of the M_{LT} phase; (a) viewed along the molecular long axis and (b) projection on the *ab* plane. Solid arrows indicate direction of the molecular motion from M_{HT} to M_{LT} phases; dashed arrows stand for that from M_{LT} to M_{HT} phases.

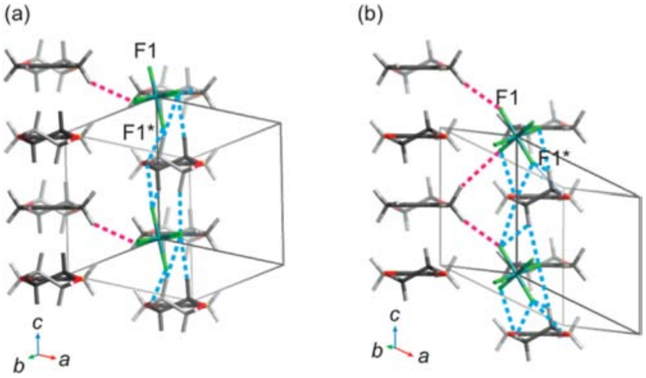

Figure 10. Donor−anion interactions for $(DMEDO\text{-}TTF)_2PF_6$ in (a) the M_{HT} phase and (b) M_{LT} phases. Blue dotted lines indicate H···F hydrogen bonds between the hydrogen atoms of the ethylene bridge and the fluorine atoms; pink dotted lines indicate H···F interaction between the hydrogen atoms of the methyl groups and the fluorine atoms.

phase is nearly perpendicular to the molecular plane, where the symmetry operator (*) implies (−*x*, −*y*, −*z*). In contrast, this axis is tilted from the *c* axis in the M_{LT} phase. The calculated tilt angles between the donor plane and the F1−P−F1* axis are 79° for the M_{HT} phase and 58° for the M_{LT} phase. There are many H···F hydrogen bonds between the ethylene bridge and the fluorine atoms. The ethylene bridge of DMEDO-TTF shows an ordered conformation in the M_{LT} phase but disordered in the M_{HT} phase. It is interesting to compare the ethylene ordering temperatures for ethylenedioxy- and ethylenedithio-substituted TTF derivatives. The ordering of the terminal ethylene is occasionally observed in the BEDT-TTF salts.[32] In these cases, the orderings take place at around 100 K in general and the intermolecular interactions between the hydrogen atoms on $-SCH_2-$ group and counter components are not distinct even below the ordering temperature in contrast with the MM transition of $(DMEDO\text{-}TTF)_2PF_6$. This tendency is consistent with the atomic electronegativities of sulfur and oxygen, that is, the resultant acidity of CH_2 groups. In other words, $-OCH_2-$ group is able to form more pronounced H···F hydrogen bonds with the anion molecules than $-SCH_2-$ group. It should be noted that the MM transition temperatures of the present compounds are higher than the usual ethylene ordering temperatures (about 100 K) of BEDT-TTF salts. The resulting rotation of the anion molecule brings about the reconstruction of the H···F interactions between the methyl groups of the neighboring column and the fluorine atoms. This type of H···F interaction is weak, but often plays a crucial role in molecular packing of crystals.[33] In (*o*-DMTTF)$_2$X (*o*-DMTTF = *o*-dimethyl-TTF, X = Cl, Br, and I), a unique molecular arrangement with a tetragonal symmetry has been realized by the characteristic H···X interaction.[34] The unique H···F interactions between the methyl groups and the fluorine atoms lead to the rearrangement of the donor packing to the square-like lattice, cooperatively with the direct donor—donor interactions. Therefore, the MM transition originates from the ordering of the ethylene bridge. The associated anion rotation results in the reconstruction of H···F interactions between the methyl groups and the anions. Accordingly, the coexistence of the ethylenedioxy and methyl groups is necessary to the structural transition. Such a dramatic structural transition is rare in BEDT-TTF, but very common in donors containing an ethylendioxy moiety,[6,26] except BO which shows the self-assembling nature.[18] The dramatic structural transitions make the TTF derivatives with ethylenedioxy group attractive for exploring the multiple physical properties.

The M$_{LT}$ phase of the SbF$_6$ salt has very similar geometrical parameters to those of the M$_{LT}$ phase of the PF$_6$ and AsF$_6$ salt, and is also a square-like lattice, as exemplified by small $\phi = 0.8°$ and $z = 0.09$ Å for *p*1 and *p*2 (Table 2). The ethylene bridge of the DMEDO-TTF molecule is disordered with two conformations, but the fraction of the major orientation is 0.63(1). The major orientation is the same as the ordered conformation of the M$_{LT}$ phase of the PF$_6$ and the AsF$_6$ salts. Although the geometrical parameters for the intracolumnar interactions *c*1 and *c*2 are unchanged between the M$_{HT}$ and M$_{LT}$ phases, the *z* values for *p*1 and *p*2 change to 1.00 and 1.06 Å in the M$_{HT}$ phase. These values are, however, smaller than those of the M$_{HT}$ phase of the PF$_6$ and AsF$_6$ salts (~ 2.2 Å), so the M$_{HT}$ phase of the SbF$_6$ salt is considerably different from the M$_{HT}$ phase of the PF$_6$ and AsF$_6$ salts.

3.5. Band Calculation.

Figure 11 shows the energy bands and the Fermi surface of the M$_{HT}$ and M$_{LT}$ phase of the PF$_6$ salt calculated on the basis of the tight-binding approximation using the intermolecular overlap integrals of HOMO obtained from the extended Hückel molecular orbital calculation.[25] The Fermi surfaces of the AsF$_6$ and SbF$_6$ salts are in essence the same as that of the PF$_6$ salt (Figure S8 in Supporting Information), although the M$_{HT}$ phase of the SbF$_6$ is, to some extent, different from those of the PF$_6$ and AsF$_6$ salts. The largest interchain transfer *p*1 of the M$_{HT}$ phase is about one-seventh of the intrachain interactions *c*1 and *c*2, so that the calculated Fermi surface is relatively flat. The interchain transfers *a*, *p*1, and *p*2 are larger in the M$_{LT}$ phase, and the average of *p*1 and *p*2 for the largest interchain direction is about one-third of the intrachain interactions. In general, HOMO of the TTF derivatives is distributed on the central TTF part and the coefficients of the HOMO in a DMEDO-TTF molecule are concentrated on the sulfur atoms of the TTF skeleton (Figure 5), where the HOMO of a DMEDO-TTF molecule is calculated by DFT method using B3LYP/6-31G(d,p).[28] The *x* values of *a*, *p*1, and *p*2 are smaller in the M$_{LT}$ phase than those of the M$_{HT}$ phase, and overlap of the HOMOs between the neighboring molecules tends to be enhanced by diminishing the *x* values. In addition, the eight coordinations in the square-like lattice generate the new *p*3 interaction. As a consequence, the 7:1 anisotropy in the M$_{HT}$ phase reduces to 3:1 in the M$_{LT}$ phase. The Q1D Fermi surface with considerable warping, however, is still susceptible to the nesting vector of $(a^* + b^*)/2$ and the MI transition at 50 K is associated with the density wave instability.

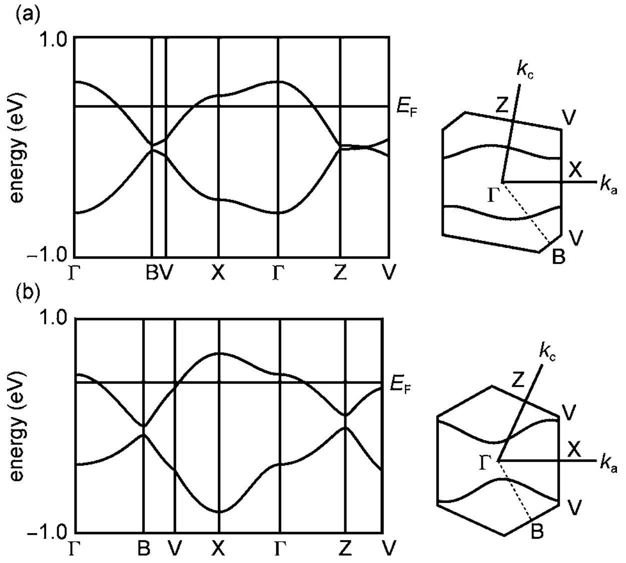

Figure 11. Enegry band structure and the Fermi surface of the (a) M$_{HT}$ and (b) M$_{LT}$ phases of the PF$_6$ salt.

3.6. Phase Diagram.

Considering these results, the phase diagram is depicted as shown in Figure 12, where the horizontal axis V_A is the anion volume estimated from the literature method.[35] The T_{MM} changes largely depending on V_A, suggesting that the MM transition is related to the donor-anion interaction or the change of the lattice volume. The number of neighboring molecules is inherent in the size and shape of organic molecules. This contrasts with inorganic materials in which the number of bonds or the coordination number determines the network. As an origin of the unusual square-lattice-like network, the driving force of the structural transition comes from the order of the ethylene bridge and the presence of characteristic H···F hydrogen bonds from the anions to not only the ethylene bridge but also the methyl

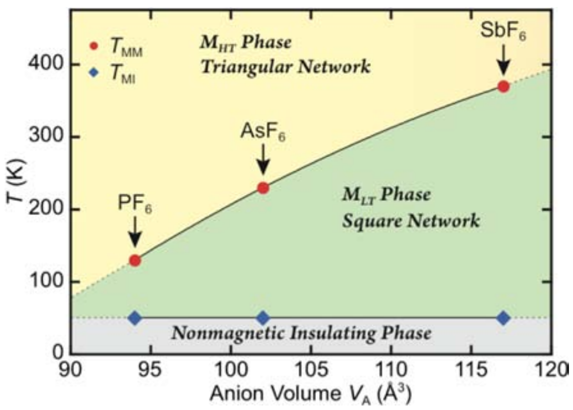

Figure 12. Phase diagram of the (DMEDO-TTF)$_2$XF$_6$ (X = P, As, and Sb). Anion volumes V_A are estimated from a following equation: $V_A = (r_i + 2r_o)^3$, where r_i and r_o indicate the inner and outer ion radii of the octahedral anions, according to the precedent of similar system.[35]

groups. Note that the structural transitions of the present compounds are based on a very sensitive balance of the triangular and square molecular arrangements. The ground state of $(DMEDO\text{-}TTF)_2XF_6$ (X = P, As, and Sb) is a nonmagnetic insulator. At this stage, the mechanism of the MI transition is attributable to the CDW instability with small charge disproportionation. The T_{MI} is independent of V_A, in contrast to the strong V_A dependence of T_{MM}. Since the M_{LT} phase has large interchain interactions, it is rather surprising that the low-temperature ground state is a nonmagnetic state. In the two-dimensional systems like the BEDT-TTF salts, whether the low-temperature insulating state is magnetic or nonmagnetic is uniquely determined from the crystal symmetry,[31b] and a system with two molecules in a unit cell, like the present system, is always a paramagnetic insulator. This does not apply to one-dimensional conductors, where the CDW state is a relevant instability in any time. In other words, the present system resembles the TMTTF salts, where the ground state is the spin-Peierls state, rather than the BEDT-TTF salts. Probably this discrepancy stems from the uniqueness of the square-like molecular arrangement, which has not been explored previously. Many important aspects like the coordination number and the triangular instability are different in the square lattice, and considerably different physics is to be investigated in order to entirely understand the M_{LT} phase.

4. CONCLUSIONS

In summary, we have prepared new molecular conductors $(DMEDO\text{-}TTF)_2XF_6$ (X = As and Sb) as a related material of the quasi-one-dimensional molecular conductor $(EDO\text{-}TTF)_2PF_6$. The first-order MM transition is accompanied by the dramatic structural change from a quasi-triangular lattice to a quasi-square-like molecular arrangement. It is noteworthy that the MM transition is associated with the order of the ethylenedioxy moiety, where more pronounced hydrogen bonds between the ethylenedioxy hydrogens and the anions give rise to the rotation of the anions and the rearrangement of the donor network owing to the unique H···F interactions between the methyl groups and the anions. These results indicate the possibility for the stimuli-responsive molecular conductors by utilizing the multistability between the triangular and the square molecular arrangements of these compounds. The ground state below 50 K is, however, a nonmagnetic insulator, and the MI transition temperature is basically independent of the anions. These results are of particular significance because the extraordinary structural transitions and the associated change of the physical properties are largely different from the standard model of the conventional organic conductors, and the present materials provide an excellent playground to explore the multifunctional properties.

■ ASSOCIATED CONTENT

Ⓢ Supporting Information

Crystallographic data in CIF format, crystal structure of DMEDO-TTF, ESR spectra of $(DMEDO\text{-}TTF)_2PF_6$, extended Hückel parameters, DSC trace of $(DMEDO\text{-}TTF)_2AsF_6$, complete ref 28, temperature dependence of lattice parameters of $(DMEDO\text{-}TTF)_2AsF_6$, definition of geometrical parameters, calculated Fermi surfaces of $(DMEDO\text{-}TTF)_2XF_6$ (X = As and Sb) and video of crystal destruction during MM transition of $(DMEDO\text{-}TTF)_2PF_6$. This material is available free of charge via the Internet at http://pubs.acs.org.

■ AUTHOR INFORMATION

Corresponding Author

shirahata.takashi.mj@ehime-u.ac.jp

Notes

The authors declare no competing financial interest.

■ ACKNOWLEDGMENTS

The authors are grateful to Dr. K. Takai and Prof. T. Enoki (Tokyo Institute of Technology) for their kindness in using SQUID magnetoromater (Quantum Design MPMS-5) and Mr. Y. Matsubara and Mr. M. Kitayama for their kind assistance of the optical property measurements. This work is partially supported by a Grant-in-Aid for Scientific Research (Nos. 18GS0208, 15073215, 19740202, 20110006, 21750148, and 23550155) from the Ministry of Education, Culture, Sports, Science and Technology, Japan, and Japan Society for the Promotion of Science. T.S. was a JSPS research fellow (Research Fellowships for Young Scientists Program, JSPS-19006916).

■ REFERENCES

(1) *Low-Dimensional Molecular Metals*; Toyota, N., Lang, M., Müller, J.; Springer-Verlag: Berlin, 2007.

(2) *TTF Chemistry: Fundamentals and Applications of Tetrathiafulvalene*; Yamada, J., Sugimoto, T., Eds.; Kodansha Springer: Tokyo, 2004.

(3) *Organic Superconductors*, 2nd ed.; Ishiguro, T., Yamaji, K., Saito, G., Eds.; Springer-Verlag: Heidelberg, 1998.

(4) For the comprehensive reviews, see the following entire issue (a) *Chem. Rev.* **2004**, *104* (11). (b) *Sci. Technol. Adv. Mater.* **2009**, *10* (2).

(5) (a) Jérome, D. *Science* **1991**, *252*, 1509−1514. (b) Itoi, M.; Kano, M.; Kurita, N.; Hedo, M.; Uwatoko, Y.; Nakamura, T. *J. Phys. Soc. Jpn.* **2007**, *76*, 053703−1−5. (c) Itoi, M.; Araki, C.; Hedo, M.; Uwatoko, Y.; Nakamura, T. *J. Phys. Soc. Jpn.* **2008**, *77*, 023701−1−4. (d) Iwase, F.; Sugiura, K.; Furukawa, K.; Nakamura, T. *J. Phys. Soc. Jpn.* **2009**, *78*, No. 104717-1−7.

(6) Ota, A.; Yamochi, H.; Saito, G. *J. Mater. Chem.* **2002**, *12*, 2600−2602.

(7) Aoyagi, S.; Kato, K.; Ota, A.; Yamochi, H.; Saito, G.; Suematsu, H.; Sakata, M.; Takaka, M. *Angew. Chem., Int. Ed.* **2004**, *43*, 3670−3673.

(8) Drozdova, O.; Yakushi, K.; Yamamoto, K.; Ota, A.; Yamochi, H.; Saito, G.; Tashiro, H.; Tanner, D. B. *Phys. Rev. B* **2004**, *70*, No. 075107-1−8.

(9) Chollet, M.; Guerin, L.; Uchida, N.; Fukaya, S.; Shimoda, H.; Ishikawa, T.; Matsuda, K.; Hasegawa, T.; Ota, A.; Yamochi, H.; Saito, G.; Tazaki, R.; Adachi, S.; Koshihara, S. *Science* **2005**, *307*, 86−89.

(10) Onda, K.; Ogihara, S.; Yonemitsu, K.; Maeshima, N.; Ishikawa, T.; Okimoto, Y.; Shao, X.; Nakano, Y.; Yamochi, H.; Saito, G.; Koshihara, S. *Phys. Rev. Lett.* **2008**, *101*, No. 067403-1−4.

(11) Yamochi, H.; Koshihara, S. *Sci. Technol. Adv. Mater.* **2009**, *10*, 024305-1−6.

(12) Shao, X.; Nakano, Y.; Yamochi, H.; Dubrovskiy, A. D.; Otsuka, A.; Murata, T.; Yoshida, Y.; Saito, G.; Koshihara, S. *J. Mater. Chem.* **2008**, *18*, 2131−2140.

(13) Shao, X.; Nakano, Y.; Sakata, M.; Yamochi, H.; Yoshida, Y.; Maesato, M.; Uruichi, M.; Yakushi, K.; Murata, T.; Otsuka, A.; Saito, G.; Koshihara, S.; Tanaka, K. *Chem. Mater.* **2008**, *20*, 7551−7562.

(14) Shao, X.; Yoshida, Y.; Nakano, Y.; Yamochi, H.; Sakata, M.; Maesato, M.; Otsuka, A.; Saito, G.; Koshihara, S. *Chem. Mater.* **2009**, *21*, 1085−1095.

(15) Murata, T.; Shao, X.; Nakano, Y.; Yamochi, H.; Uruichi, M.; Yakushi, K.; Saito, G.; Tanaka, K. *Chem. Mater.* **2010**, *22*, 3121−3132.

(16) Fabre, J. M.; Serhani, D.; Saoud, K.; Chakroune, S.; Hoch, M. *Synth. Met.* **1993**, *60*, 295−298.

(17) Fabre, J. M.; Chakroune, S.; Javidan, A.; Zanik, L.; Ouahab, L.; Golhen, S.; Delhaes, P. *Synth. Met.* **1995**, *70*, 1127−1129.

(18) Yamochi, H. *Oxygen Analogues of TTFs in TTF Chemistry: Fundamentals and Applications of Tetrathiafulvalene*; Yamada, J., Sugimoto, T., Eds.; Kodansha Springer: Tokyo, 2004; Chap. 4, pp 83−118.

(19) (a) Laukhina, E; Vidal-Gancedo, J.; Laukhin, V.; Veciana, J.; Chuev, I.; Tkacheva, V.; Wurst, K.; Rovira, C. *J. Am. Chem. Soc.* **2003**, *125*, 3948−3953. (b) Shibaeva, R. P.; Yagubskii, E. B. *Chem. Rev.* **2004**, *104*, 5347−5378.

(20) Phillips, D. C.; Mathews, F. S.; North, A. C. T. *Acta Cryst.* **1968**, *A24*, 351−359.

(21) *SAINT*; Version 7.60A; Bruker AXS, Inc.: Madison, WI, 1997−2009.

(22) Sheldrick, G. M. *SADABS: Program for Empirical Absorption Correction*; University of Gottingen: Gottingen, Germany, 1996.

(23) Burla, M. C.; Caliandro, R.; Camalli, M.; Carrozzini, B.; Cascarano, G. L.; De Caro, L.; Giacovazzo, C.; Polidori, G.; Siliqi, D.; Spagna, R. *SIR2008: Program for the Solution of Crystal Structures from X-ray Data*; CNR Institute of Crystallography: Bari, Italy, 2007.

(24) Sheldrick, G. M. *SHELXL (SHELX97): Program for the Refinement of Crystal Structures*; University of Gottingen: Gottingen, Germany, 1996.

(25) Mori, T.; Kobayashi, A.; Sasaki, Y.; Kobayashi, H.; Saito, G.; Inokuchi, H. *Bull. Chem. Soc. Jpn.* **1984**, *57*, 627−633.

(26) Shirahata, T.; Kibune, M.; Imakubo, T. *J. Mater. Chem* **2005**, *15*, 4399−4402.

(27) Moser, J.; Gabay, M.; Auban-Senzier, P.; Jérome, D.; Bechgaard, K.; Fabre, J. M. *Eur. Phys. J. B* **1998**, *1*, 39−46.

(28) Normal mode and MO calculations were carried out with the DFT/TD-DFT method at the B3LYP/6-31g(d,p) level using Gaussian 03 program package. Frisch, M. J. *Gaussian 03*, revision C.02; Gaussian, Inc.: Wallingford, CT, 2004.

(29) Mori, T. *Bull. Chem. Soc. Jpn.* **1998**, *71*, 2509−2526.

(30) Jerome, D.; Mazaud, A.; Ribault, M.; Bechgaard, K. *J. Phys., Lett.* **1980**, *41*, L95−L98.

(31) (a) Mori, T.; Mori, H.; Tanaka, S. *Bull. Chem. Soc. Jpn.* **1999**, *72*, 179−197. (b) Mori, T. *Bull. Chem. Soc. Jpn.* **1999**, *72*, 2011−2027.

(32) (a) Geiser, U.; Schults, A. J.; Wang, H. H.; Watkins, D. M.; Stupka, D. L.; Williams, J. M.; Schirber, J. E.; Overmyer, D. L.; Jung, D.; Novoa, J. J.; Whangbo, M.-H. *Physica C* **1991**, *174*, 475−486. (b) Geiser, U.; Wang, H. H.; Schlueter, J. A.; Williams, J. M.; JSmart, L.; Cooper, A. C.; Kumar, S. K.; Caleca, M.; Dudek, J. D. *Inorg. Chem.* **1994**, *33*, 5101−5107. (c) Schultz, A. J.; Wang, H. H.; Williams, J. M.; Filhol, A. *J. Am. Chem. Soc.* **1986**, *108*, 7853−7855.

(33) Fourmigué, M.; Batail, P. *Chem. Rev.* **2004**, *104*, 5379−5418.

(34) Fourmigué, M.; Reinheimer, E. W.; Dunbar, K. R.; Auban-Senzier, P.; Pasquier, C.; Coulon, C. *Dalton Trans.* **2008**, 4652−4658.

(35) Williams, J. M.; Beno, M. A.; Sullivan, J. C.; Banovetz, L. M.; Braam, J. M.; Blackman, G. S.; Carlson, C. D.; Greer, D. L.; Loesingt, D. M. *J. Am. Chem. Soc.* **1983**, *105*, 643−645.